Reducing Model-Discrepancy in High-Fidelity Structural Simulators Using Advanced Nonlinear Theories for Digital Twinning

Reducing Model-Discrepancy in High-Fidelity Structural Simulators Using Advanced Nonlinear Theories for Digital Twinning

Gaetano Miraglia*[1][0000-0002-3611-0215] and Rosario Ceravolo[1][0000-0001-5880-8457]

[1] Politecnico di Torino, Turin TO 10129, IT
*gaetano.miraglia@polito.it

Abstract. The mechanical modelling of masonry systems is notoriously challenging due to the wide behaviour that such structures can exhibit when subjected to random external forcing. Several laws have been proposed in the past for this purpose, with the result, however, of being: (i) too accurate of a specific structural behaviour, with the risk of losing the physical meaning or overfitting the experimental data; or on the contrary (ii) too approximate, which, even if efficient, only able to capture some global characteristics of the mechanical behaviour.
In the present work, the authors propose the use of a recent continuum theory, which instead of describing the structural problem in differential form, uses nonlinear integral-differential equations of motion having a limited number of mechanical parameters. This continuum theory, called *Peridynamics*, however, when used in a discrete sense must be corrected in order to reduce the discrepancy that arises in approximating the continuity of the body. In the present study, the authors propose a method to overcome this discrepancy that arises in using low resolution simulators instead of high-resolution ones.

Keywords: Digital Twin, Masonry structures, Nonlinear models, Peridynamics, Structural simulators.

1 Introduction

Finding the right balance between accuracy and computational efficiency of structural simulators is essential to obtain valuable information on the health state of real structures in a feasible computational time. In reaching this balance, the parallel use of low fidelity and high fidelity structural models is helpful, being the first approach ideal to extract very fast information, while the second able to generate high quality knowledge on complex behaviours of real systems. However, if Structural Health Monitoring (SHM) techniques need to be applied to a large number of structures (e.g., urban

area), very high-fidelity models result to be inadequate to obtain information in a feasible computational time.

Peridynamics (PDs) is a modern nonlocal theory of continuum established in early 2000 by Stewart Silling [1], [2] and Silling et al. [3]. The theory is recently attracting attention in the field of computational mechanics since it replaces the partial differential equations of the classical continuum theory with integral, spatial equations. This allows overcoming problems related to the representation of discontinuities in the matter, which can arise during damage (e.g., cracks), where the differential formulations are not defined. A comprehensive literature review of PD applications and uses can be found in [4]. PD is thus a candidate theory that can be used for modelling real systems.

About the modelling of real systems, the work of Gosliga and Worden [5] is noteworthy. Here the authors propose the use of *Irreducible Element* (IE) *model*, which seeks to create a graphical representation of a system (using graph theory [6], [7], [8]) by breaking it down into its constituent parts, with the aim to assess the similarity of structures. The system modelling plays an important role in the SHM of existing systems [9], [10]. In this field, Farrar and Worden et al. have done important research [11], [12], [13], while the promising future of this discipline is also dictated by the technological advancement of the last years [14].

1.1 Research significant

The importance of the research lies in the fact that PDs is a promising theory for modelling masonry structures, and more generally in the use of the theory for the structural monitoring of this kind of systems driven by models based on physical behaviour (i.e., ultra-high-fidelity models, or digital twins). This is true for two reasons: (i) the theory is formulated starting from an elegant mathematical framework that guarantees the representation of strong non-linearities (e.g., rocking, crack propagation, etc.); (ii) the representation of these nonlinearities is reached with a reduced number of mechanical parameters, which in turn maintain a simple and straightforward physical meaning. However, computational models that are too expensive could generate problems during the digital twinning phase (due to the long times required for twinning). For this reason it is useful to use low-fidelity (or low resolution) PD models. When following this path, however, it is necessary to pay attention to a series of problems related to the modelling discrepancy that is created with respect to the PD continuum theory, such as the onset of strong surface effects, or problems of integration of the restoring forces related to a too coarse discretization.

The paper aims to correct these discrepancies that arise when using low resolution models, thus ensuring high accuracy of the results accompanied by minimal computational effort, making the digital twinning of masonry structures affordable.

Section 2 reports the proposed methods to correct the model discrepancy, Section 3 describes the analyses performed to validate the methods, while in Section 4 the results of the analyses are discussed. In Section 5, the conclusions are drawn.

2 Methods

In this section, after a brief introduction of the basic concepts of PDs, the proposed discrepancy correction method is presented.

2.1 Basics of Peridynamics

Basically, PD theory found its principle in the forces-interaction (*bonds*) of points. The matter is divided into infinitesimal portions characterized by their mass and volume. Each point *k* is then supposed to interact with its neighbours inside a region. The collection of all the points inside this region is called *family* of *k*. The family of *k* is, in turn, characterized by the *horizon*, i.e., the maximum distance for which the interactions between *k* and the other points of a body occur. The horizon defines the locality of the behaviour of a system; the smaller the horizon, the more local the behaviour will be. It has been demonstrated that the classical theory of elasticity can be considered as a limiting case of the PD theory as the horizon approaches zero [15], [16], [17].

When using PD in a modelling phase, the choice of the horizon represents a crucial aspect. It can be a constant or variable along the modelling space. In other cases the value of the horizon is not defined, and its definition should be based on calibration procedures [18]. When the nonlocal theory is used to model damage (e.g., crack growth and propagation), several works have related the value of the horizon with the value of the average distance between points used to discretize the continuum, [19], [20]. In this case, the horizon is commonly set to three times the spacing between points. Among the different types of PD theory, in the present work the Bond Based PD (BBPD) is assumed.

The linearized micro-linear viscoelastic BBPD equation of motion can be written in standard form as (bold is herein used for vectors, bold capital for matrices and italic for scalars):

$$\mathbf{M}\ddot{\mathbf{u}}(t) + \mathbf{C}\dot{\mathbf{u}}(t) + \mathbf{K}\mathbf{u}(t) = \mathbf{z}(t)$$

$$\mathbf{M} = \begin{bmatrix} \mathbf{M}_k & \mathbf{O}_3 & \dots \\ \mathbf{O}_3 & \ddots & \cdots \\ \vdots & \vdots & \ddots \end{bmatrix};\ \mathbf{C} = \begin{bmatrix} \sum_{\substack{j=1 \\ j\neq k}}^{K} \mathbf{C}_{kj} & -\mathbf{C}_{kj} & \dots \\ -\mathbf{C}_{kj} & \ddots & \dots \\ \vdots & \vdots & \ddots \end{bmatrix};\ \mathbf{K} = \begin{bmatrix} \sum_{\substack{j=1 \\ j\neq k}}^{K} \mathbf{K}_{kj} & -\mathbf{K}_{kj} & \dots \\ -\mathbf{K}_{kj} & \ddots & \dots \\ \vdots & \vdots & \ddots \end{bmatrix} \tag{1}$$

where:

$$
\begin{aligned}
\mathbf{M}_k &= m_k \mathbf{I}_3 \\
\mathbf{C}_{kj} &= \nu_{kj} \mathbf{K}_{kj} \\
\mathbf{K}_{kj} &= c_{kj} V_j V_k \boldsymbol{\Xi}_{kj} \\
\boldsymbol{\Xi}_{kj} &= \frac{\boldsymbol{\xi}_{kj} \left(\boldsymbol{\xi}_{kj}{}^{\mathrm{T}}\right)}{\left\|\boldsymbol{\xi}_{kj}\right\|^3} \\
c_{kj} &= \begin{cases} c_{kj} \text{ if } \left\|\boldsymbol{\xi}_{kj}\right\| \leq h \\ 0 \text{ if } \left\|\boldsymbol{\xi}_{kj}\right\| > h \end{cases} \\
\boldsymbol{\xi}_{kj} &= \mathbf{x}_j - \mathbf{x}_k
\end{aligned}
\tag{2}
$$

In Eq. (1) and Eq. (2) $\mathbf{x}_k = (x_{k,X}, x_{k,Y}, x_{k,Z})^{\mathrm{T}}$ are the coordinates *X*, *Y*, *Z* of point *k* (similarly for *j*), $c_{kj} \geq 0$ is called bond elastic constant, and *h* is the horizon. V_j and V_k are the volumes, accounting for the volume corrections, associated to the points *j* and *k* respectively while $\nu_{kj} \geq 0$ is a bond damping constant; m_k is the mass associated to the point *k*, $\mathbf{I}_3$ is a 3x3 identity matrix and $\mathbf{O}_3$ is a 3x3 zero matrix. *K* is the number of points of the network used to discretize the system. Then, $\mathbf{u}(t)$ and $\mathbf{z}(t)$ denote the displacement vector and the external force vector respectively, being *t* the time variable and $\dot{(\ldots)}(t)$ the time derivate operator. Finally, **M**, **C**, and **K** denote the mass, damping, and stiffness global matrices of the system.

In addition to the quantities reported in Eq. (1) and Eq. (2), for nonlinear analysis the following quantities must be defined:

$$
\begin{aligned}
\mathbf{y}_k &= \mathbf{x}_k + \mathbf{u}_k \\
s_{kj}\left(\mathbf{u}_j - \mathbf{u}_k, \mathbf{x}_j - \mathbf{x}_k, t\right) = s_{kj}(t) &= \frac{\left\|\mathbf{y}_j(t) - \mathbf{y}_k(t)\right\| - \left\|\mathbf{x}_j - \mathbf{x}_k\right\|}{\left\|\mathbf{x}_j - \mathbf{x}_k\right\|}
\end{aligned}
\tag{3}
$$

where in Eq. (3), $\mathbf{u}_k(t)$ is a sub-component of $\mathbf{u}(t) = (\mathbf{u}_1(t), \mathbf{u}_k(t), \ldots)^T$, s_{kj} is defined as bond stretch, while $\mathbf{y}_k$ is the deformed coordinates vector for point *k*. In addition the following applies:

$$
\begin{aligned}
&\cdot \text{when } s_{kj}(t) \leq 0 \quad \rightarrow \quad c_{kj}(t) = c_{kj} \\
&\cdot \text{when } s_{kj}(t) > 0 \;\; and \; if \;\; s_{kj}(t^{\mathrm{o}}) > s_0 \quad \rightarrow \\
&c_{kj}(t) = \delta^{\mathrm{o}}{}_{kj} c_{kj} \quad \text{where} \quad \delta^{\mathrm{o}}{}_{kj} = \begin{cases} 1 \; for \; 0 < t < t^{\mathrm{o}} \\ 0 \; for \; t \geq t^{\mathrm{o}} \end{cases}
\end{aligned}
\tag{4}
$$

where in Eq. (4), s_0 is called critical bond stretch. In this work, in order to account for collapsing in compression, as can happen to masonry structures, the following modification of Eq. (4) is proposed:

$$\begin{aligned} &\cdot \text{when } s_{kj}(t) \le 0 \;\; and\, if \;\; s_{kj}(t') < \; s_1 \rightarrow \\ &c_{kj}(t) = \delta'_{kj} c_{kj}(0) \;\; \text{where} \;\; \delta'_{kj} = \begin{cases} 1 \; for \; 0 < t < t' \\ 0 \; for \; t \ge t' \end{cases} \\ &\cdot \text{when } s_{kj}(t) > 0 \;\; and\, if \;\; s_{kj}(t^{\circ}) > \; s_0 \;\; \rightarrow \\ &c_{kj}(t) = \delta^{\circ}{}_{kj} c_{kj}(0) \;\; \text{where} \;\; \delta^{\circ}{}_{kj} = \begin{cases} 1 \; for \; 0 < t < t^{\circ} \\ 0 \; for \; t \ge t^{\circ} \end{cases} \end{aligned} \tag{5}$$

where in Eq. (5), s_0 represents the critical bond stretch in tension, while s_1 is the proposed critical bond stretch in compression.

2.2 Proposed discrepancy correction method

The proposed discrepancy correction method aims to maintain the Young's modulus of the system unchanged in the presence of surface effects and/or too coarse discretization problems which can affect the integration of the bond elastic constant on the volume of the horizon. The method is summarised in the following algorithm:

1. Initialize *i*=0, the assumed value of the Young's modulus vector $\mathbf{E_{true}}$ with dimension (*K*x1), and the discrepancy correction vector $\mathbf{r}_i$ as a unitary vector (*K*x1);
2. Estimate the bond elastic constant matrix $\mathbf{B} = \mathbf{r}_i \circ \mathbf{1} \circ \frac{4\mathbf{E_{true}}}{A2h \cdot h}$ (for mono dimensional models), $\mathbf{B} = \mathbf{r}_i \circ \mathbf{1} \circ \frac{9\mathbf{E_{true}}}{\pi h^2 a \cdot h}$ (for bi-dimensional models), and $\mathbf{B} = \mathbf{r}_i \circ \mathbf{1} \circ \frac{16\mathbf{E_{true}}}{(4/3)\pi h^3 \cdot h}$ (for tri-dimensional models), where *A* is the cross section surface of the model, *a* is the thickness of the model and **1** is a unitary matrix with dimension (*K*x*K*), (°) indicates the *Hadamard* product (or in general operator) between a vector and a matrix;
3. Applies the volume correction method proposed by [21] and get the corrected volume matrix **V** with dimension (*K*x*K*). **V** is a sparse matrix where each *k-th* row contains the corrected volumes (correction that consider the ratio of the volume of the points on the border of the family of *k*) of the *J* points in the family of *k*. The points that are out of the family of *k* have zero volumes at the *k-th* rows;
4. Modify **B** as follow: $\mathbf{B} = \frac{\mathbf{B}+\mathbf{B}^T}{2}$;
5. Estimate the Young's modulus vector (dimension *K*x1) as: $\mathbf{E} = \frac{h}{4}\sum_{j=1}^{K}\left(\mathbf{b}_j \circ \mathbf{v}_j\right)$ (for mono dimensional models), $\mathbf{E} = \frac{h}{9}\sum_{j=1}^{K}\left(\mathbf{b}_j \circ \mathbf{v}_j\right)$ (for bi-

dimensional models), and $\mathbf{E} = \frac{h}{16}\sum_{j=1}^{K}\left(\mathbf{b}_j \circ \mathbf{v}_j\right)$ (for tri-dimensional models), where $\mathbf{b}_j$ and $\mathbf{v}_j$ are the *j-th* columns of the matrix **B** and **V**, respectively;

6. Update the free variable $i=i+1$;
7. Calculates the new value of the discrepancy correction vector as: $\mathbf{r}_i = \mathbf{r}_{i-1} \circ \mathbf{E}_{\mathbf{true}} \circ \mathbf{E}^{\circ -1}$;
8. Start recursively from point 2.;
9. Stop when $\mathbf{E}_{\mathbf{true}} - \mathbf{E}$ is close to the zero vector and $\mathbf{B} - \mathbf{B}^T$ is close to the zero matrix.

3 Applications

In order to demonstrate the proposed model discrepancy correction method for PD models, a benchmark structure has been supposed. It consists of a wall with 1x1 m of area, and thickness of 0.1 m (see Fig. 1 left). The Young's modulus is equal to 4.21×10^9 Pa, the Poisson ratio equal to 0.25, and density equal to 1800 kg/m^3. The critical bond stretch in tension is equal to 2.518×10^{-4}, while the critical bond stretch in compression equal 1.221×10^{-3}. The bound damping constant is equal to 0.003 s, while the bound elastic constant is calculated as described in Section 2 starting from the Young's modulus value. A horizontal displacement time history $d(t)$, where t denotes time, has been applied to half of the wall (see Fig. 1 right). The assumption is that $d(t)$ is positive if put in tension the wall (from the left to the right), negative if put in compression the wall (from the right to the left). The wall is fully restrained on the vertical left edge.

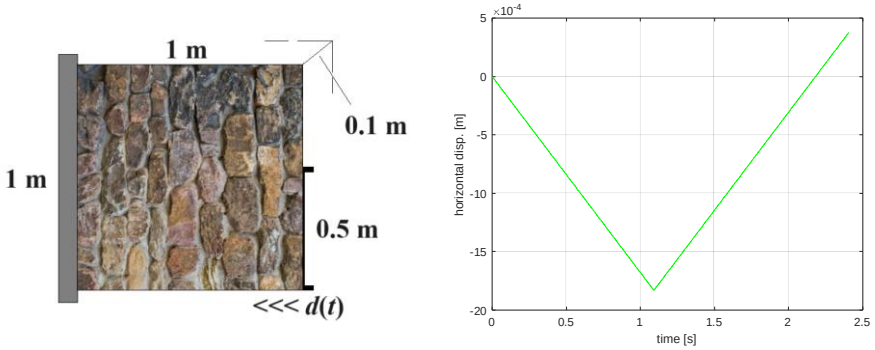

Fig. 1. Benchmark system (on the left) and applied horizontal displacement time history $d(t)$ (on the right).

3.1 Reference system verification with eigen-analysis via Finite Element Model

In order to define a correct mesh size that is representative of the theoretical problem, but that at the same time ensures computational efficiency, a sensitivity analysis of the mesh size to the modal problem was conducted via Finite Element (FE) analysis using

4 nodes plate elements with two Degree of Freedoms (DoFs) per node (i.e., horizontal, and vertical displacements) that implement the plane stress theory with thickness definition. The mesh size was initially set to a very small value a priori, i.e., 0.001 m, which defined the *high-resolution* FE model. The first natural frequency of vibration was tracked against the mesh dimension and the optimal size was defined to 0.05 m (which defined the assumed FE model, or Model 0). This value of the mesh size allows for a high accuracy and a relatively null computational effort.

In Fig. 2 the meshed models, the 5th mode shape of the high-resolution FE model (mesh size of 0.001 m) and the 5th mode shape of the assumed FE model for the study (mesh size of 0.05 m) are depicted, while the values of the first natural frequencies of both modelling are reported in Table 1.

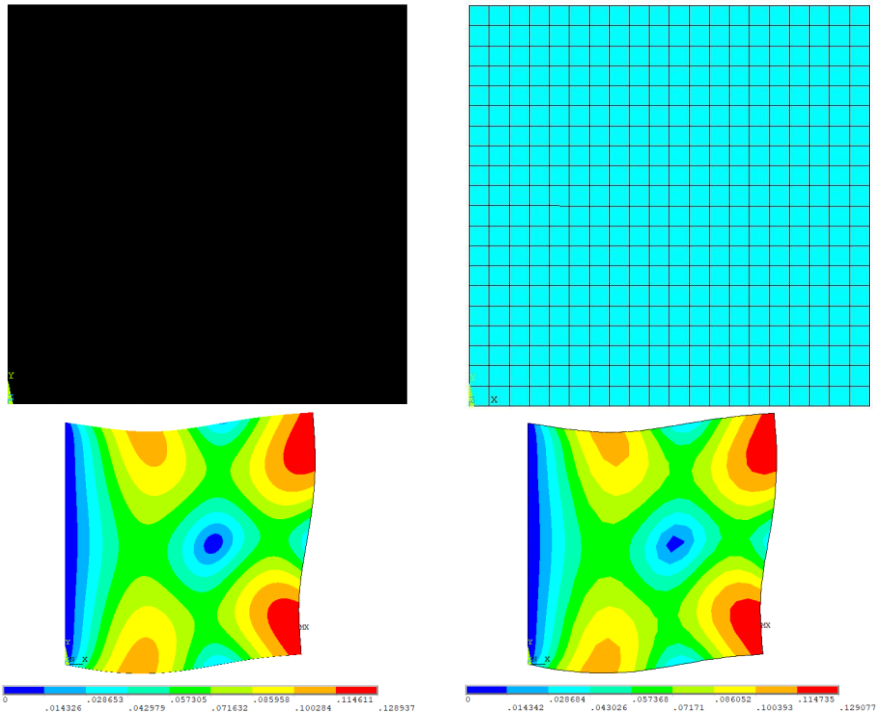

Fig. 2. High-resolution FE model (top left), Model 0 (top right), 5th mode shape predicted by the high-resolution FE model (bottom left), and 5th mode shape predicted by Model 0 (bottom right).

Table 1. Comparison between the first five natural frequencies predicted by the high-resolution FE model and Model 0.

Nat. freq. [Hz]	High-resolution FE model	Assumed FE model (Model 0)
1	161.37	161.54
2	383.89	383.89

3	435.17	434.71
4	687.78	684.01
5	751.47	751.14

Given the mesh size of 0.05 m of the assumed FE model (Model 0), a PD model with the same value of the distance between the points of the network was realized. The obtained PD model may represent the reference model for the nonlinear analysis. However, in order to take the model as reference is necessary to verify it in linear elastic field. The verification has been performed by comparing the natural frequencies obtained with the classical continuum theory and those ones obtained by the PD theory.

As can be observed from Table 2, the PD model without discrepancy correction (Model 1) provide a wrong representation of the modal behaviour, instead the corrected PD model (Model 2) correctly fit the values of natural frequency estimated with the classical continuum theory with negligible errors. For these reasons, from now on the reference model becomes the corrected PD model with distance between points equal to 0.05 m (Model 2), which in linear elastic field coincide, less than a small error due to horizon choice, to the assumed FE model (Model 0). Fig. 3 reports the reference model of the study, with the first, the fourth and the fifth mode shapes predicted by the PD theory.

Table 2. Natural frequency prediction of Model 0, Model 1, and Model 2, with relative errors with respect to Model 0 prediction.

Nat. freq. [Hz]	Assumed FE model (Model 0)	Non corrected peridynamic model (Model 1)	Relative error from Model 0 [%]	Corrected peridynamic model (Model 2)	Relative error from Model 0 [%]
1	161.54	132.77	-17.81	159.17	-1.47
2	383.89	321.35	-16.29	374.04	-2.57
3	434.71	356.59	-17.97	424.95	-2.25
4	684.01	544.43	-20.41	682.98	-0.15
5	751.14	612.84	-18.41	704.18	-6.25

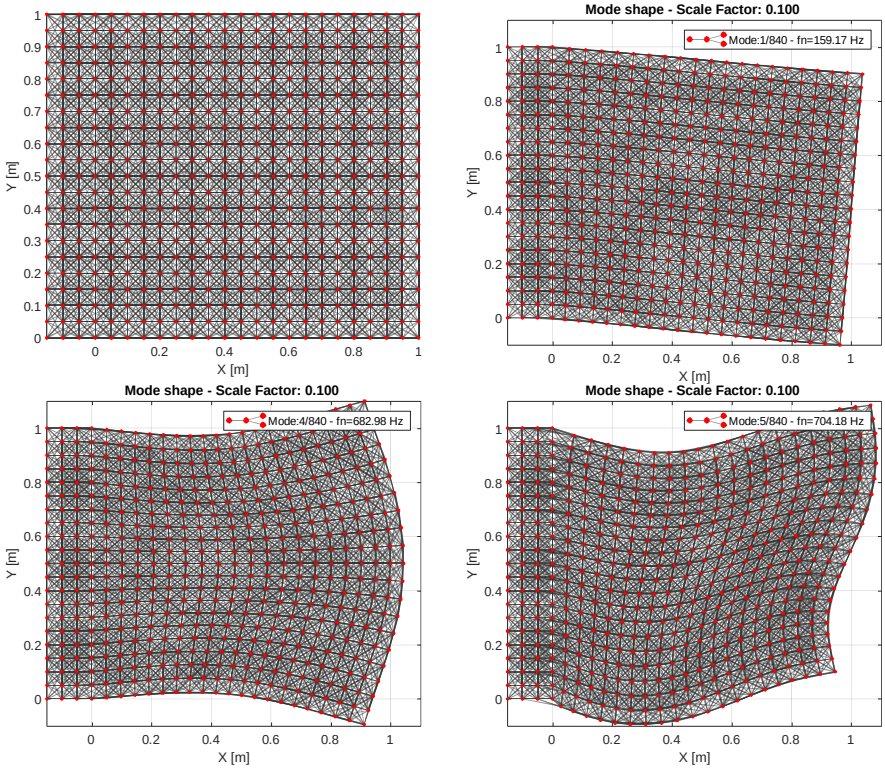

Fig. 3. Reference peridynamic model, i.e., Model 2 (top left), and mode shapes predicted by Model 2.

3.2 Performed analyses

In order to verify the proposed discrepancy correction method, six models were realized with different values of distance between the points of the network, but with same mechanical properties. For half of the models the proposed correction method was not applied:

- Model 0: FE model with a mesh size of 0.05 m.
- Model 1: PD model with distance between points 0.05 m, correction not applied.
- Model 2: PD model with distance between points 0.05 m, correction applied.
- Model 3: PD model with distance between points 0.1 m, correction not applied.
- Model 4: PD model with distance between points 0.1 m, correction applied.
- Model 5: PD model with distance between points 0.125 m, correction not applied.
- Model 6: PD model with distance between points 0.125 m, correction applied.

For the PD analysis the load was applied to a *non-zero real volume* of the model, with an extension equal to the distance between the points of the network. Instead, the

boundary condition was applied to a *non-zero virtual volume* for an extension equal to the horizon value, i.e., three times the distance between the points of the network. Two types of analysis were conducted, i.e., eigen-analysis and nonlinear analysis. For the nonlinear analysis, the implemented time-step integration method is the implicit Newmark method with average acceleration.

Eigen-analysis

For the eigen-analysis all the modes of vibration predicted by the PD models were extracted, however just the first five values of natural frequency are reported in the work (for space reasons). Table 3 reports the time needed to run the eigen-analyses.

Table 3. Time necessary to get the results of the eigen-analyses.

Computational time [s]	Model 1	Model 2 (ref.)	Model 3	Model 4	Model 5	Model 6
Intel(R) Xeon(R) W-2255 CPU @ 3.70GHz 3.70 GHz, RAM 256 GB	~2.57	~2.26	~0.64	~0.39	~0.51	~0.54

Nonlinear analysis

For the nonlinear analyses, a displacement time history was applied to the bottom half of the depth of the wall. The length of the signal is 2.405 s (i.e., 1605 samples). Table 4 reports the time needed to run the nonlinear analyses. Since the analyses contemplate different distances between points of the networks, the comparison of the results reported in the contour plots on the following pages have been interpolated on a common basis; a surface having a regular distance between points equal to 0.01 m.

Table 4. Time necessary to get the results of the nonlinear analyses.

Computational time [s]	Model 1	Model 2 (ref.)	Model 3	Model 4	Model 5	Model 6
Intel(R) Xeon(R) W-2255 CPU @ 3.70GHz 3.70 GHz, RAM 256 GB	~18167	~2109	~156	~152	~35	~68

4 Results and discussion

In the present section, the results of the performed analyses are commented. In particular, the comparison between the output provided by the corrected models and the uncorrected ones are critically analysed at the end of the section.

4.1 Analysis without discrepancy correction

In this subsection the results of the uncorrected models are presented.

Eigen-analysis

Fig. 4 reports the results of the eigen-analysis for Model 1, 3, and 5 in terms of natural frequencies and 5th mode shape predicted by the models.

Nat. freq. [Hz]	Model 1	Model 3	Model 5
1	132.77	119.49	113.44
2	321.35	291.73	277.32
3	356.59	320.67	303.16
4	544.43	471.07	436.35
5	612.84	544.37	510.47

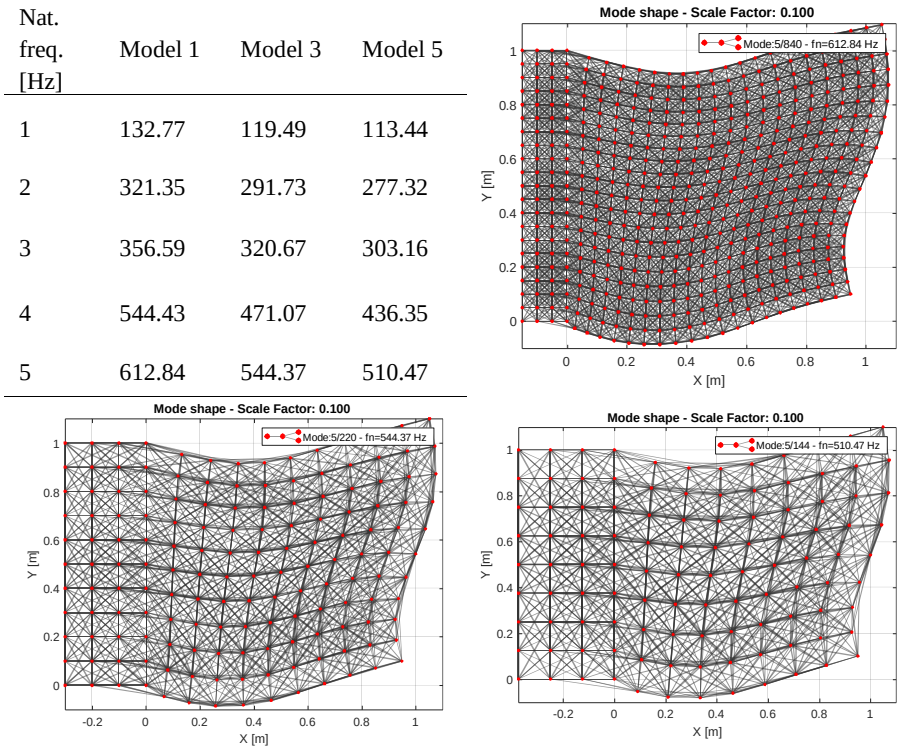

Fig. 4. Results of the eigen-analysis. Natural frequencies predicted by the models (top left), mode shape of the 5th mode predicted by Model 1 (top right), mode shape of the 5th mode predicted by Model 3 (bottom left), mode shape of the 5th mode predicted by Model 5 (bottom right).

The results show that the models significantly underestimate the actual natural frequencies values. Instead, the mode shapes are well represented even without discrepancy correction. This strongly depend by the geometry of the study. In more detail, it means that the discrepancy is uniformly distributed over the space (e.g., uniform surface effects around the free boundaries).

Nonlinear analysis

Fig. 5 and Fig. 6 report the results of the nonlinear analysis for Model 1 and 5 in terms of reaction force vs applied displacement, damaged bond stretches, Young's modulus distribution, and maximum absolute average bond stretch distribution.

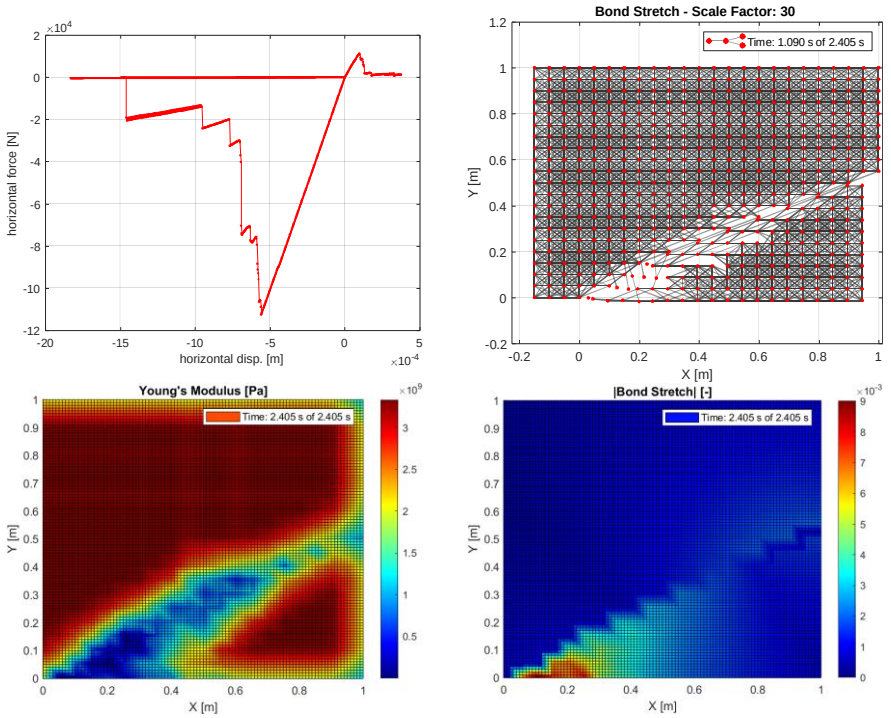

Fig. 5. Results of the nonlinear analysis for Model 1. Total reaction force vs applied displacement (top left), damaged bond stretches @ 1.090 s (top right), minimum Young's modulus distribution reached at the end of the analysis (bottom left), maximum absolute average bond stretch distribution reached at the end of the analysis (bottom right).

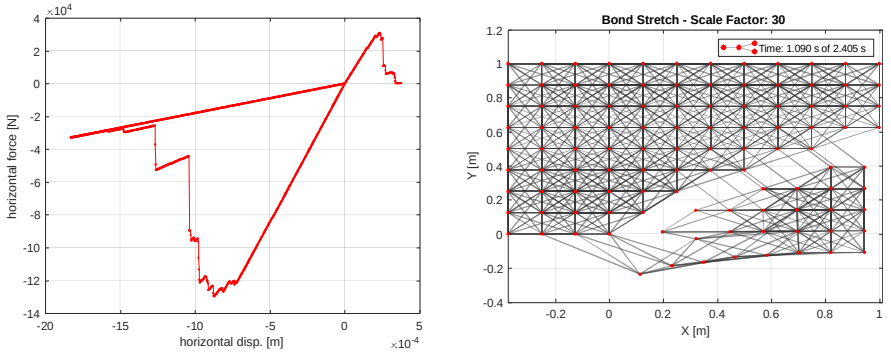

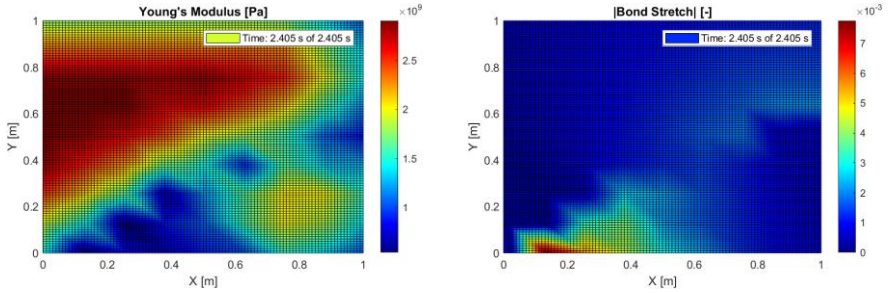

Fig. 6. Results of the nonlinear analysis for Model 5. Total reaction force vs applied displacement (top left), damaged bond stretches @ 1.090 s (top right), minimum Young's modulus distribution reached at the end of the analysis (bottom left), maximum absolute average bond stretch distribution reached at the end of the analysis (bottom right).

The results show that all the models suffer from surface effects as can be perceived from the values of the Young's modulus at the free boundary of the system. In addition, the integration of the bond elastic constant over the volume occupied by the horizon did not bring to a correct value of the young's modulus inside the body. As regards the comparison of the outcomes obtained from the different models, it is possible to detect a tendency of the damage to incorrectly propagate to a wider area when the distance between the points of the network increases.

4.2 Analysis with discrepancy correction

In this subsection the results of the corrected models are presented.

Eigen-analysis

Fig. 7 reports the results of the eigen-analysis for Model 2, 4, and 6 in terms of natural frequencies and 5th mode shape predicted by the models.

Nat. freq. [Hz]	Model 2	Model 4	Model 6
1	159.17	156.24	154.37
2	374.04	366.38	361.73
3	424.95	417.78	412.56
4	682.98	663.20	646.95
5	704.18	668.17	650.79

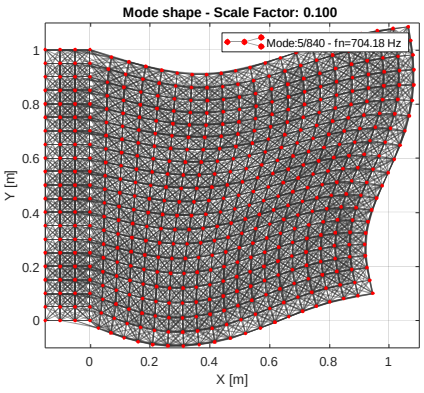

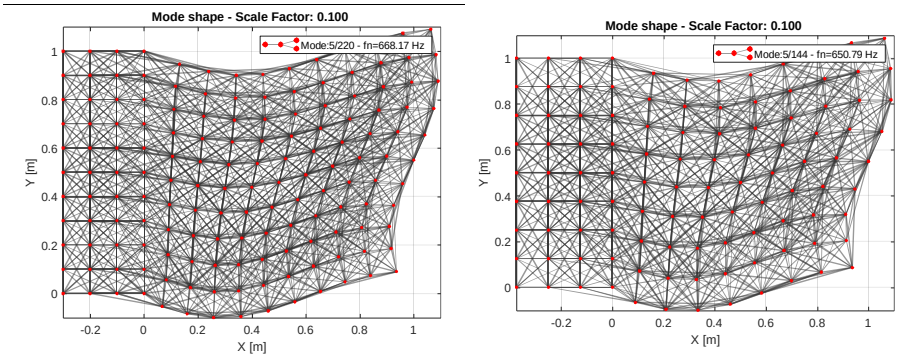

Fig. 7. Results of the eigen-analysis. Natural frequencies predicted by the models (top left), mode shape of the 5th mode predicted by Model 2 (top right), mode shape of the 5th mode predicted by Model 4 (bottom left), mode shape of the 5th mode predicted by Model 6 (bottom right).

The results show that the models correctly estimate both natural frequency values and mode shapes (with a little underestimate), with low discrepancy with respect to the results obtained by Model 0 (assumed FE model).

Nonlinear analysis

Fig. 8 and Fig. 9 report the results of the nonlinear analysis for Model 2 and 6 in terms of reaction force vs applied displacement, damaged bond stretches, Young's modulus distribution, and maximum absolute average bond stretch distribution.

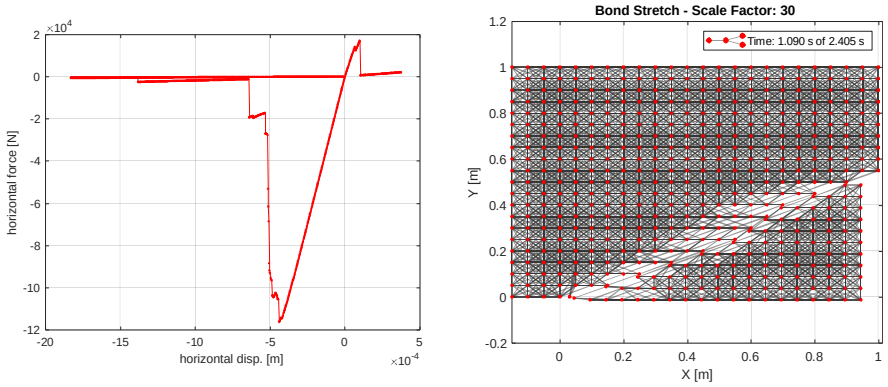

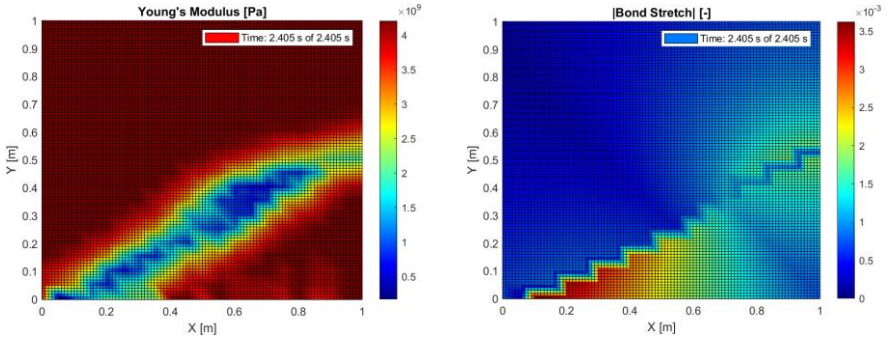

Fig. 8. Results of the nonlinear analysis for Model 2 (reference model). Total reaction force vs applied displacement (top left), damaged bond stretches @ 1.090 s (top right), minimum Young's modulus distribution reached at the end of the analysis (bottom left), maximum absolute average bond stretch distribution reached at the end of the analysis (bottom right).

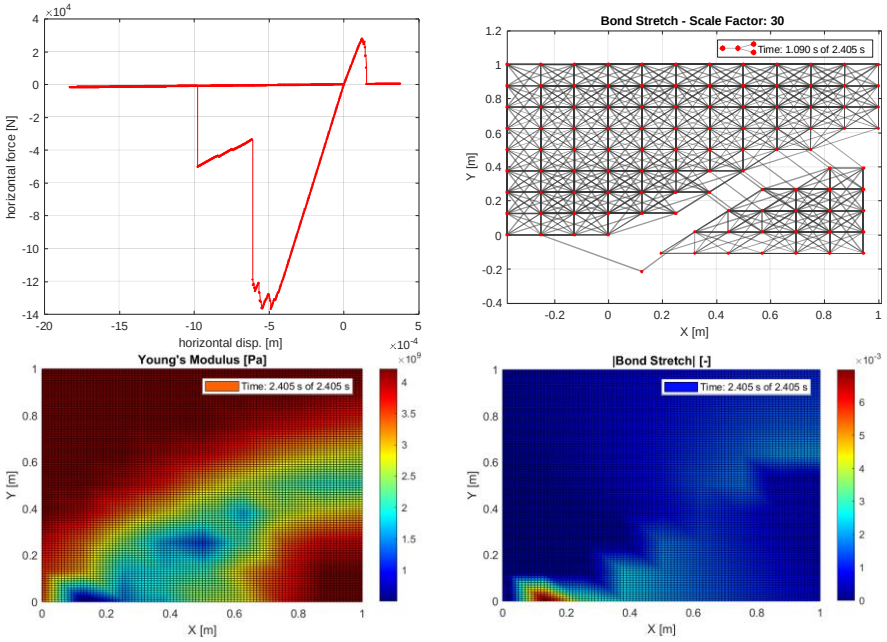

Fig. 9. Results of the nonlinear analysis for Model 6. Total reaction force vs applied displacement (top left), damaged bond stretches @ 1.090 s (top right), minimum Young's modulus distribution reached at the end of the analysis (bottom left), maximum absolute average bond stretch distribution reached at the end of the analysis (bottom right).

The results show that all the models do not suffer from surface effects as can be perceived from the values of the Young's modulus at the free boundary of the system. In

addition, the integration of the bond elastic constant over the volume occupied by the horizon brought to a correct value of the young's modulus inside the body.

As regards the comparison of the outcomes obtained from the different models, even in this case it is possible to detect a tendency of the damage to incorrectly propagate to a wider area when the distance between the points of the network increases, however, in contrast to the outcomes of Model 1, 3, and 5, now the damaged area is more stable with respect to an increases of the distance between the points of the network, instead, a little discrepancy is still visible in the reaction force vs applied displacement curve.

4.3 Quantitative comparison

Fig. 10 depicts the errors obtained by the different assumed modelling strategies, instead the numerical values of the errors are reported in Table 5.

The error was calculated in terms of Normalized Root Mean Square Error (NRMSE), where for natural frequencies the normalization is performed in terms of natural frequencies predicted by Model 2, while for total reaction force, Young's modulus, and bond stretch distribution the normalization is performed in terms of maximum amplitude (i.e., difference between maximum and minimum value) predicted by Model 2 due to the time-variant nature of these characteristics, which can take on zero value.

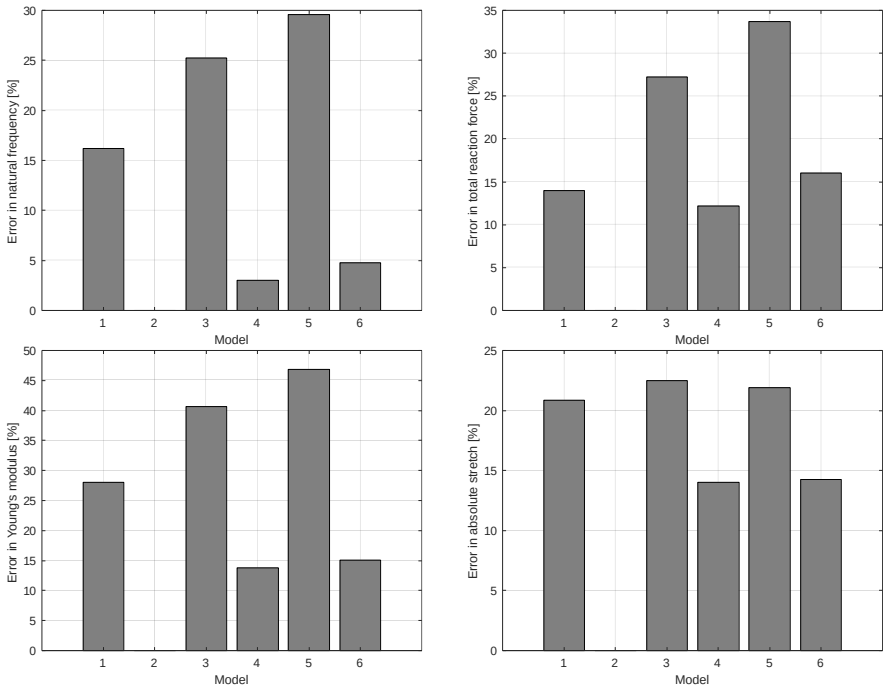

Fig. 10. Errors in terms of natural frequency (top left), total reaction force (top right), Young's modulus distribution (bottom left), and bond stretch (bottom right) for the assumed models.

Table 5. Values of absolute error in terms of natural frequency, total reaction force, Young's modulus, and bond stretch distribution for the assumed models.

Quantity [%]	Model 1	Model 2 (ref.)	Model 3	Model 4	Model 5	Model 6
Natural frequency	16.20	0	25.24	2.99	29.58	4.77
Total reaction force	13.99	0	27.22	12.16	33.67	16.01
Young's modulus	28.02	0	40.63	13.75	46.88	15.03
Bond stretch	20.84	0	22.51	13.99	21.91	14.24

From the results of the analyses, it is possible to conclude that the proposed discrepancy correction method significantly contributes to reducing errors in the estimate of the natural frequencies, reaction force, Young's modulus, and bond stretch distribution. This is related to the correct estimate of the elastic properties obtained after the correction procedure (see Fig. 11). In more detail, the corrected models present a lower variation of the errors with respect to that obtained by the non-corrected models.

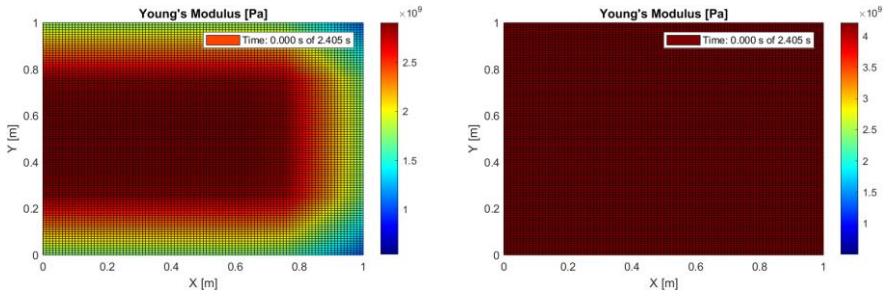

Fig. 11. Initial Young's modulus distribution for Model 5 (left) and Model 6 (right). The correction procedure brings to a correct estimate of the Young's modulus over the structure (i.e., 4.21×10^9 Pa).

5 Conclusions

In the paper, a micro-viscoelastic BBPD constitutive law with resistance and degradation in compression, and a correction method for modelling errors was proposed to reduce the discrepancy that occur when a low-resolution peridynamic model is used instead of a high-resolution model (e.g., surface effects increase, etc.).

It was demonstrated that the method significantly reduces the discrepancy, and in addition, it makes the peridynamic model in more agreement with the classical continuum theory (except for residual discrepancy due to the horizon value choice). The correction is based on the concept of stiffness and consists in varying the bond elastic constant from its nominal value, in order to keep the Young's modulus of the material unchanged.

This allows the use of low-fidelity (low resolution) models without a substantial decrease in accuracy with respect to that one obtained from a high-resolution model, but with the advantage of reducing the computational effort of one/two orders of magnitude, making digital twinning more affordable.

It is worth underling that in the nonlinear field, the different resolution of representation also leads to a different instantaneous energy release when a bond breaks. The higher the distance between the points of the network, the higher the energy released. This further source of modelling discrepancy will be the subject of a future work, in continuation of what is presented in this work and in line with the Hy-Learn project (https://www.polito.it/en/polito/communication-and-press-office/poliflash/young-researchers-pnrr-call-seven-young-postdocs-at-the).

Acknowledgments

The presented work is part of the activities carried out within the Hy-Learn project PNRR Young Researchers "Seal of Excellence."

References

1. Silling SA (2000) Reformulation of elasticity theory for discontinuities and long-range forces. J Mech Phys Solids 48:175–209
2. Silling SA (2001) Peridynamic modeling of the Kalthoff--Winkler experiment. Submission for the 2001 Sandia Prize in Computational Science
3. Silling SA, Epton M, Weckner O, Xu J, Askari E (2007) Peridynamic states and constitutive modeling. J Elast 88:151–184
4. Javili A, Morasata R, Oterkus E, Oterkus S (2019) Peridynamics review. Mathematics and Mechanics of Solids 24:3714–3739
5. GOSLIGA J, WORDEN K (2019) A General Representation for Assessing the Similarity of Structures. Structural Health Monitoring 2019
6. Bondy JA, Murty USR, others (1976) Graph theory with applications. Macmillan London
7. West DB, others (2001) Introduction to graph theory. Prentice hall Upper Saddle River
8. Sanderson DJ, Peacock DCP, Nixon CW, Rotevatn A (2019) Graph theory and the analysis of fracture networks. J Struct Geol 125:155–165
9. Sohn H, Farrar CR, Hemez FM, Shunk DD, Stinemates DW, Nadler BR, Czarnecki JJ (2003) A review of structural health monitoring literature: 1996--2001. Los Alamos National Laboratory, USA 1–7
10. Amezquita-Sanchez JP, Adeli H (2019) Nonlinear measurements for feature extraction in structural health monitoring. Scientia Iranica 26:3051–3059
11. Rogers TJ, Worden K, Fuentes R, Dervilis N, Tygesen UT, Cross EJ (2019) A Bayesian non-parametric clustering approach for semi-supervised Structural Health Monitoring. Mech Syst Signal Process 119:100–119

12. Farrar CR, Worden K (2007) An introduction to structural health monitoring. Philosophical Transactions of the Royal Society A: Mathematical, Physical and Engineering Sciences 365:303–315
13. Farrar CR, Worden K (2012) Structural health monitoring: a machine learning perspective. John Wiley & Sons
14. Sony S, Laventure S, Sadhu A (2019) A literature review of next-generation smart sensing technology in structural health monitoring. Struct Control Health Monit 26:e2321
15. Madenci E, Oterkus E (2014) Peridynamic theory and its applications. Springer
16. Silling SA, Zimmermann M, Abeyaratne R (2003) Deformation of a peridynamic bar. J Elast 73:173–190
17. Weckner O, Abeyaratne R (2005) The effect of long-range forces on the dynamics of a bar. J Mech Phys Solids 53:705–728
18. Bobaru F, Foster JT, Geubelle PH, Silling SA (2016) Handbook of peridynamic modeling. CRC press
19. Madenci E, Oterkus E (2014) Peridynamic theory and its applications. Springer
20. Bobaru F, Foster JT, Geubelle PH, Silling SA (2016) Handbook of peridynamic modeling. CRC press
21. Madenci E, Oterkus E (2014) Peridynamic theory and its applications. Springer